

Defect-assisted tunneling spectroscopy of electronic band structure in twisted bilayer graphene/hexagonal boron nitride moiré superlattices

Cite as: Appl. Phys. Lett. **120**, 203103 (2022); <https://doi.org/10.1063/5.0084996>

Submitted: 11 January 2022 • Accepted: 06 May 2022 • Published Online: 18 May 2022

Yuta Seo,  Satoru Masubuchi, Momoko Onodera, et al.



View Online



Export Citation



CrossMark

ARTICLES YOU MAY BE INTERESTED IN

Transmission electron microscopy at the quantum limit

Applied Physics Letters **120**, 190502 (2022); <https://doi.org/10.1063/5.0086148>

Spin-polarized transport properties of the FeCl₂/WSe₂/FeCl₂ van der Waals heterostructure

Applied Physics Letters **120**, 203505 (2022); <https://doi.org/10.1063/5.0091580>

Direct bandgap GeSn nanowires enabled with ultrahigh tension from harnessing intrinsic compressive strain

Applied Physics Letters **120**, 202103 (2022); <https://doi.org/10.1063/5.0087477>

Lock-in Amplifiers
up to 600 MHz



Zurich
Instruments



Defect-assisted tunneling spectroscopy of electronic band structure in twisted bilayer graphene/hexagonal boron nitride moiré superlattices

Cite as: Appl. Phys. Lett. **120**, 203103 (2022); doi: [10.1063/5.0084996](https://doi.org/10.1063/5.0084996)

Submitted: 11 January 2022 · Accepted: 6 May 2022 ·

Published Online: 18 May 2022



View Online



Export Citation



CrossMark

Yuta Seo,¹ Satoru Masubuchi,¹ Momoko Onodera,¹ Rai Moriya,¹ Yijin Zhang,¹ Kenji Watanabe,² Takashi Taniguchi,^{1,3} and Tomoki Machida^{1,a)}

AFFILIATIONS

¹Institute of Industrial Science, University of Tokyo, 4-6-1 Komaba, Meguro-ku, Tokyo 153-8505, Japan

²Research Center for Functional Materials, National Institute for Materials Science, 1-1 Namiki, Tsukuba 305-0044, Japan

³International Center for Materials Nanoarchitectonics, National Institute for Materials Science, 1-1 Namiki, Tsukuba 305-0044, Japan

^{a)}Author to whom correspondence should be addressed: tmachida@iis.u-tokyo.ac.jp

ABSTRACT

We report the demonstration of defect-assisted tunneling spectroscopy of the electronic band structure in twisted bilayer graphene (tBLG)/hexagonal boron nitride (*h*-BN) moiré superlattices in which the moiré period between the two graphene layers is close to that between the graphene and *h*-BN layers. We measured both the in-plane and vertical carrier transport in the tBLG/*h*-BN van der Waals (vdW) tunneling device. The moiré periods were determined from the in-plane carrier transport measurements. The observed vertical tunneling transport characteristics indicated that resonant tunneling occurs from the graphite electrode to tBLG through localized defect states in the *h*-BN tunnel barrier. We observed multiple defect-assisted resonant tunneling trajectories, from which we derived the density of states (DOS) for tBLG. The obtained DOS has broad flatband features, in qualitative agreement with the theoretical predictions. Furthermore, we obtained three types of DOS, suggesting that we probed local band structures corresponding to AA, AB/BA, and domain wall sites in tBLG. Thus, defect-assisted tunneling spectroscopy has potential as a tool to determine the local band structures in twisted 2D vdW materials.

Published under an exclusive license by AIP Publishing. <https://doi.org/10.1063/5.0084996>

When two graphene layers are stacked with a small twist angle, a moiré interference pattern with hexagonal symmetry emerges at the graphene-graphene interface due to the slight misorientation between the lattices. The electronic bands of the two graphene layers hybridize into a strongly modified twist-angle-dependent band structure. In particular, when the twist angle between the two graphene layers is close to the so-called magic angle of $\sim 1.05^\circ$, flat electronic bands are formed around the charge neutrality point (CNP). Intriguing novel phenomena have been observed in magic-angle twisted bilayer graphene (tBLG).^{1–3}

When magic-angle tBLG is placed on hexagonal boron nitride (*h*-BN) with a small misorientation angle, its electronic structures are further reconstructed owing to the moiré superlattice potential induced at the *h*-BN-tBLG interface. When one of the graphene layers is crystallographically aligned with the *h*-BN layer, the moiré period induced by the interference between the graphene and *h*-BN lattices is

nearly equal to that between the two graphene layers. As a result, the flat bands of tBLG are expected to be significantly altered by the moiré perturbation. A theoretical investigation⁴ showed that the flat bands in tBLG are broadened and in some cases overlap with higher-energy dispersive bands. Experimentally, orbital ferromagnetism and an anomalous Hall effect were observed in closely aligned magic-angle tBLG/*h*-BN.^{5,6}

Furthermore, lattice relaxation in tBLG results in moiré lattice reconstruction to minimize the total energy. At small twist angles in particular, the AA stacking area shrinks and triangular domain structures with alternating AB/BA stacking regions are formed, resulting in drastic changes in the electronic band structure.^{7,8} Spectroscopy for investigating such a strongly localized and correlated system requires a probe with high spatial and spectral resolution that interacts only minimally with tBLG. Indeed, scanning tunneling spectroscopy (STS) of tBLG has unveiled unique atomic-scale structural and electronic properties.^{9–18}

Resonant tunneling through an impurity/defect level in van der Waals (vdW) tunnel barrier can also fulfill these requirements. It has been observed that the tunneling conductance is enhanced when the carrier tunnels through a defect level in *h*-BN, and this effect can be utilized to realize graphene excitation spectroscopy.^{21,22,24} Since its defect states are highly localized on the nanometer scale, defect-assisted tunneling is effective as a local probe of the band structure of graphene.

In this study, we demonstrated the feasibility of defect-assisted tunneling spectroscopy in tBLG moiré superlattices [Fig. 1(a)]. For this proof of concept demonstration, a *h*-BN/tBLG/thin *h*-BN/graphite/*h*-BN vdW heterostructure device [Fig. 1(b)] was fabricated via the vdW pickup method and robotic assembly.^{25,26} The moiré periods between the two graphene layers and that between graphene and *h*-BN layers were $\lambda_{G-G} \sim 14$ nm and $\lambda_{G-BN} \sim 13$ nm, and the corresponding twist angles were $\theta_{G-G} = 1.0^\circ$ and $\theta_{G-BN} \sim 0.5^\circ$, respectively. The twist angle between the graphene layers was precisely controlled via the tear-and-stack method^{27,28} combined with the laser pre-cutting of graphene.²⁹ The *h*-BN (four layers, 1.3-nm thick) inserted between the tBLG and graphite layers functioned as a tunnel barrier. The active tunnel junction area was $\sim 11 \mu\text{m}^2$. Top and bottom *h*-BN layers (26- and 21-nm thick, respectively) encapsulated the tBLG/thin *h*-BN/

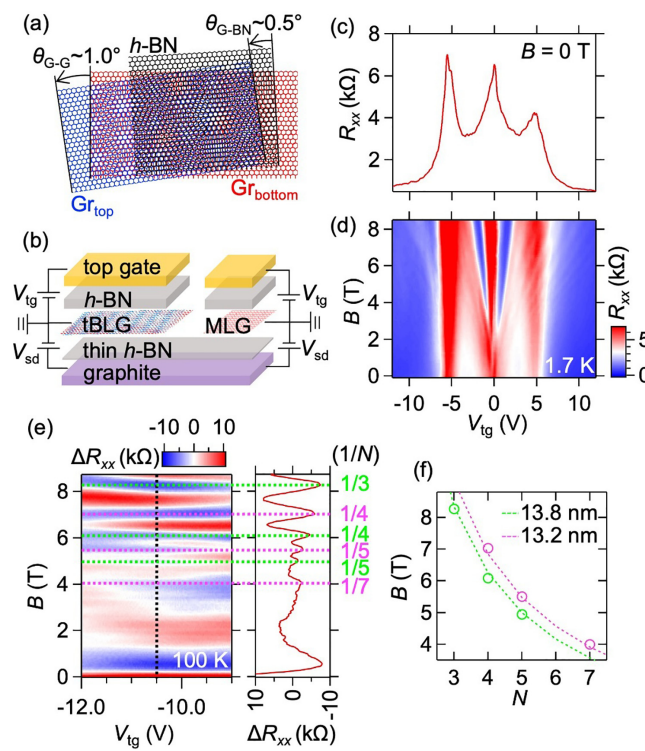


FIG. 1. (a) Schematic of tBLG/h-BN moiré superlattices. (b) Schematic of the device used in this study. (c) R_{xx} vs V_{tg} at 1.7 K. (d) Colormap of R_{xx} vs B and V_{tg} at 1.7 K. (e) Colormap of ΔR_{xx} vs B and V_{tg} at 100 K (left panel) with plot of ΔR_{xx} vs B along the dotted black line in the colormap (right panel). The horizontal dashed lines and numbers on the right show the BZ oscillations of tBLG (green) and graphene/h-BN (magenta) with different values of $1/N$ for $B = (1/N)\phi_0$. Here, N is an integer and ϕ_0 is the flux quantum. (f) Experimental (open circles) and calculated (dotted lines) B vs N for BZ oscillations in tBLG (green) and graphene/h-BN (magenta).

graphite tunnel junction. The straight edges of the top *h*-BN layer and the upper graphene layer of tBLG were aligned with a small misorientation angle. Our device structure was carefully designed to allow vertical tunneling transport and in-plane transport measurements to be conducted on the same area of the device. This was realized by the highly selective etching of *h*-BN using CF_4/O_2 plasma.³⁰ We also fabricated a monolayer graphene (MLG) device as a reference, incorporating one of graphene sheets used in the tBLG device [Fig. 1(b), right].

First, we characterized the tBLG/h-BN moiré superlattices in terms of their in-plane carrier transport. The theoretical relationships between the moiré periods, λ_{G-G} and λ_{G-BN} , and the twist angles, θ_{G-G} and θ_{G-BN} , are illustrated in Fig. S2 in the supplementary material. Figure 1(c) shows the longitudinal resistance R_{xx} in tBLG vs the top-gate voltage V_{tg} at a temperature T of 1.7 K. Figure 1(d) shows a colormap of R_{xx} as a function of V_{tg} and the perpendicular magnetic field B . Three peaks are apparent in this plot. The central and satellite peaks correspond to the CNP and the full filling of the flat bands in tBLG, respectively. The carrier densities at the full filling conditions are $n_{tBLG} = \pm 2.3 \times 10^{12} \text{ cm}^{-2} \equiv \pm n_s = 4/A = 8\sqrt{3}/3\lambda_{G-G}^2$, where $A = \sqrt{3}\lambda_{G-G}^2/2$ is the area of the moiré unit cell. Thus, λ_{G-G} and θ_{G-G} were determined to be ~ 14 nm and $= 1.0^\circ$, respectively [Fig. S2 open red circle in the supplementary material].

The left panel of Fig. 1(e) is a colormap of ΔR_{xx} as a function of V_{tg} and B at $T = 100$ K. This shows ΔR_{xx} oscillations in the B direction, which are known as Brown-Zak (BZ) oscillations,³¹ a manifestation of Bloch oscillation in moiré superlattices. To observe these BZ oscillations more clearly, we showed ΔR_{xx} , which was obtained by subtracting the smooth background from R_{xx} . The right panel of Fig. 1(e) is a line plot showing ΔR_{xx} along the black dotted line in the left panel. The oscillations have two different periods, $\Delta(1/B) = 0.040$ and 0.0365 T^{-1} . This observation of BZ oscillations with two independent periods confirms the existence of two moiré potentials with different periods. By contrast, BZ oscillation with a single period was observed in the MLG/h-BN reference device (see the supplementary material, Fig. S3 for the in-plane carrier transport characteristics of the reference device). The dotted lines in Fig. 1(f) are calculated values of B satisfying the BZ condition. The BZ oscillation minima plotted as open circles in Fig. 1(f) are well explained by $\lambda_{G-G} = 13.8$ nm ($\theta_{G-G} = 1.02^\circ$) and $\lambda_{G-BN} = 13.2$ nm ($\theta_{G-BN} \sim 0.53^\circ$).

Next, the vertical tunneling transport was studied. The application of a source-drain voltage V_{sd} between tBLG and graphite causes a tunnel current I to flow through the *h*-BN tunnel barrier. In earlier experiments on graphene/h-BN/graphene vdW tunnel junctions, the differential tunneling conductance dI/dV_{sd} was shown to reflect the density of states (DOS) of the graphene electrodes and the tunneling probability.³²⁻⁴⁰ In the present study, dI/dV_{sd} was obtained by differentiating the $I-V_{sd}$ curves, and the carrier density n_{tBLG} and chemical potential μ_{tBLG} of tBLG were precisely controlled by varying V_{sd} and V_{tg} .

Figure 2(a) shows a grayscale plot of dI/dV_{sd} as a function of V_{tg} and V_{sd} . Many bright lines linking from the top-center to the bottom-left and the top-center to the bottom-right are apparent. These lines are the trajectories of dI/dV_{sd} maxima. The inset shows a close-up of the area bounded by the dashed yellow line in the main plot. The trajectories cross at $V_{sd} = 0$, exhibiting diamond-like shapes reminiscent of Coulomb-blockade diamonds. These features are attributed to

resonant tunneling through a defect state in the *h*-BN barrier, as illustrated by the configuration and energy diagrams in Figs. 2(c) and 2(d). μ_{tBLG} and ϕ_{Gr} are the chemical potential of tBLG and the static potential of graphite, respectively, as measured from the CNP of tBLG. Applying V_{sd} between the tBLG and graphite layers induces a shift of eV_{sd} between μ_{tBLG} and ϕ_{Gr} . Here, we assume that a defect level is formed at the energy μ_D in the *h*-BN tunnel barrier. When μ_D is within the transport window, i.e., $\mu_{\text{tBLG}} \leq \mu_D \leq \phi_{\text{Gr}}$ [Fig. 2(d)], carriers can resonantly tunnel through the defect level, resulting in enhanced tunnel conductance. Thus, the bright lines forming diamond-like shapes near $V_{\text{sd}} = 0$ are explained as the onsets of defect-assisted resonant tunneling through the defect levels in *h*-BN, and along each line either $\mu_{\text{tBLG}} = \mu_D$ ($V_{\text{sd}} > 0$) or $\phi_{\text{Gr}} = \mu_D$ ($V_{\text{sd}} < 0$) is satisfied. Since similar defect-assisted resonant tunneling is expected to occur via other defect states, the multiple dI/dV_{sd} peak trajectories can arise from the multiple defect states in the *h*-BN tunnel barrier.

Recent studies demonstrated that even nominally pure *h*-BN crystals contain impurities and structural defects, with localized electronic states formed within the energy gap.^{19–24,41,42} Moreover, similar differential conductance peak trajectories forming Coulomb-blockade-like diamond structures were reported in MLG/*h*-BN vdW tunnel junctions,^{19,21,24,43} where the results were attributed to defect-assisted resonant tunneling and the defect density of 0.04–1 μm^{-2} and multiple defect-level formation by each defect were demonstrated. Thus, the above-mentioned assumption of the existence of multiple defect states in the thin *h*-BN tunnel barrier in the present device is reasonable.

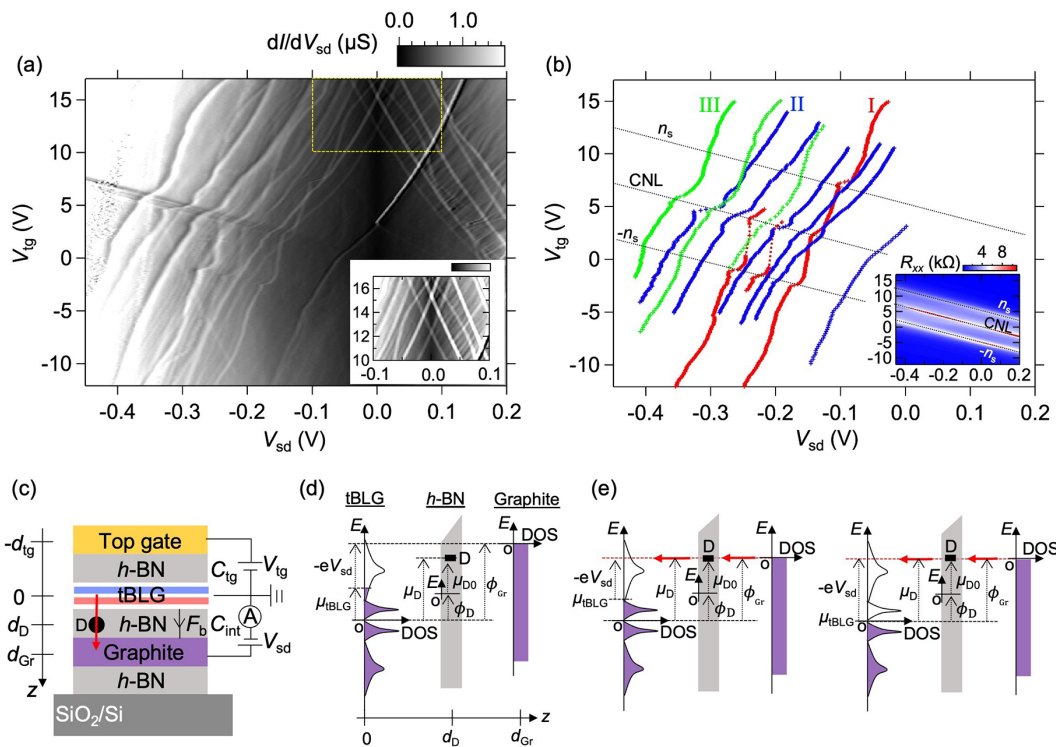


FIG. 2. (a) Grayscale plot of dI/dV_{sd} vs V_{sd} and V_g at 1.7 K. The inset is a close-up of the area bounded by the dashed yellow line in the main plot. (b) Position of dI/dV_{sd} maxima extracted from (a). The inset is a color plot of R_{xx} vs V_{sd} and V_g at 1.7 K. (c) Configuration and (d) energy diagrams. (e) Schematic diagram of defect-assisted tunneling. μ_{tBLG} is at the full filling of the flatband (left) and at the CNP (right).

Here, we focus on negative bias conditions, where $\mu_{\text{tBLG}} < \phi_{\text{Gr}}$. Multiple trajectories are apparent in the $V_{\text{sd}} < 0$ area of Fig. 2(a). The positions of the dI/dV_{sd} maxima were extracted and plotted in Fig. 2(b). The trajectories can be classified into three categories according to their shape, as indicated by the red (I), blue (II), and green (III) colors in the plot. Trajectories belonging to the same category are similar in shape and arranged parallel to each other. Each trajectory is associated with resonant tunneling through a localized defect level, thus $\phi_{\text{Gr}} = \mu_D$ as shown in Fig. 2(e). The three black dotted lines in Fig. 2(b) indicate the positions of the CNP (central line) and the full filling of the flat bands (outer lines) in tBLG, i.e., $n_{\text{tBLG}} = 0$ and $n_{\text{tBLG}} = \pm n_s$, respectively. These positions were derived from the in-plane carrier transport data shown in the inset of Fig. 2(b), where R_{xx} is plotted vs V_{tg} and V_{sd} . Along the CNP line, dI/dV_{sd} is suppressed [Fig. 2(a), dark diagonal line]. This is an influence of the tunneling into the CNP of tBLG through the bulk region of the *h*-BN barrier (see the supplementary material, Fig. S8).

We now describe the relationships among V_{tg} , V_{sd} , μ_{tBLG} , n_{tBLG} , and n_{Gr} for the configuration illustrated in Fig. 2(c) using the capacitive model:^{44,45}

$$\begin{cases} eV_{\text{sd}} = -\frac{e^2}{C_{\text{int}}}n_{\text{Gr}} + \mu_{\text{tBLG}}, \\ eV_{\text{tg}} = \frac{e^2}{C_{\text{tg}}}(n_{\text{tBLG}} + n_{\text{Gr}}) + \mu_{\text{tBLG}}, \end{cases} \quad (1)$$

where C_{int} and C_{tg} are the geometric capacitances, e is the elementary charge, and n_{Gr} is the carrier density of graphite. Since defect-assisted resonant tunneling occurs when $\phi_{\text{Gr}} = \mu_{\text{D}}$, along the trajectories it follows:

$$\begin{cases} \mu_{\text{tBLG}} = e(V_{\text{sd}} - V_{\text{sd}0}), \\ n_{\text{tBLG}} = \frac{C_{\text{tg}}}{e} [(V_{\text{tg}} - V_{\text{tg}0}) - (V_{\text{sd}} - V_{\text{sd}0})]. \end{cases} \quad (2)$$

Here, $V_{\text{sd}0}$ and $V_{\text{tg}0}$ are the values of V_{sd} and V_{tg} , respectively, when μ_{tBLG} is at the CNP of tBLG [Fig. 2(e), right panel]. Thus, these values can be determined experimentally from the intersection of each defect-assisted resonance trajectory and the CNP line of tBLG. We note that the voltage drop inside the tBLG is negligible because the tunneling resistance ($\sim 1 \text{ M}\Omega$) is much larger than the in-plane resistance of the tBLG ($< 12 \text{ k}\Omega$). The values of C_{int} and C_{tg} can also be determined experimentally by fitting to the Landau fan diagram of the MLG/h-BN reference device as $C_{\text{int}} = 1.22 \times 10^{-2} \text{ F/m}^2$ and $C_{\text{tg}} = 7.9 \times 10^{-4} \text{ F/m}^2$. Using Eq. (2), the values of V_{sd} and V_{tg} which are controlled during the tunneling experiments, can be converted to μ_{tBLG} and n_{tBLG} .

First, we focus on the trajectory labeled (I) in Fig. 2(b). The values of V_{sd} and V_{tg} along the trajectory are converted to μ_{tBLG} and n_{tBLG} using Eq. (2) and plotted as red markers in Fig. 3(a). The black solid line was obtained by interpolating the experimental data using a smoothing function. Figure 3(b) shows the DOS of tBLG, $d\mu_{\text{tBLG}}/dn_{\text{tBLG}}$, obtained by numerically differentiating the interpolated line. Figure 3(c) shows the calculated DOS and band structure of tBLG ($\theta_{\text{G-G}} = 1.0^\circ$) for comparison. The calculation was carried out based on the *ab initio* $\mathbf{k} \cdot \mathbf{p}$ perturbation continuum model proposed by Carr *et al.* using the calculation code available on GitHub.⁴⁶

In Fig. 3(a), μ_{tBLG} increases rapidly at $n_{\text{tBLG}} = 0$. This behavior is attributed to the small DOS at the CNP. The same type of rapid increase in μ_{tBLG} is seen at $n_{\text{tBLG}} = \pm n_s$, reflecting the small DOS corresponding to the full filling of the flatband [Fig. 3(b), black triangles]. By contrast, the slope of μ_{tBLG} vs n_{tBLG} is small in the regions between $n_{\text{tBLG}} = 0$ and $\pm n_s$, which correspond to the first van Hove singularity (vHs) points [Fig. 3(b), blue triangles]. In addition, at $n_{\text{tBLG}} = \pm 2n_s$,

the slope is small because of the large DOS at the second vHs points [Fig. 3(b), green triangles]. Overall, the features described above are qualitatively consistent with the calculated DOS of tBLG, which confirms the effectiveness of defect-assisted tunneling spectroscopy in tBLG.

The experimentally acquired DOS in Fig. 3(b) shows peaks (blue triangles) attributed to flatband generation between the CNP and the full filling point. These features are qualitatively consistent with features in the calculated DOS. Quantitatively, there is an apparent difference. The experimentally obtained DOS shows broadening: the width of the electron-side flatband W_+ ($\sim 40 \text{ meV}$) and that of the hole-side W_- ($\sim 30 \text{ meV}$) are much broader than the same features in the calculated DOS (15–20 meV) and slightly larger than the DOS obtained in STS experiments (tens of meV).^{9–12,47,48} These differences can be explained by considering the effect of an additional moiré superlattice potential at the *h*-BN–tBLG interface. A theoretical study⁴ indicated that close alignment with *h*-BN perturbs the band structure of tBLG near $\theta_{\text{G-G}} \sim 1^\circ$ and broadens the flat bands. In our device, tBLG and *h*-BN are closely aligned ($\theta_{\text{G-BN}} \sim 0.53^\circ$). Thus, our experimentally derived DOS features are in good agreement with theoretical predictions.

Based on the same analysis, we obtained the $\mu_{\text{tBLG}}-n_{\text{tBLG}}$ curves and derived DOS from all the resonant lines in Fig. 2(b). Figures 4(a) and 4(b), respectively, show representative $\mu_{\text{tBLG}}-n_{\text{tBLG}}$ curves and DOS plots for the three types of resonant lines denoted I (red), II (blue), and III (green) (see the supplementary material, Figs. S4–S7, for all the $\mu_{\text{tBLG}}-n_{\text{tBLG}}$ curves and DOS for each trajectory). The fact that three different shapes of DOS were obtained in the experiment indicates that at least three different types of DOS coexist in tBLG. This situation is in sharp contrast to earlier experiments on defect-assisted tunneling in conventional MLG/*h*-BN,^{19,21,24,43} where all the observed tunneling trajectories were almost identical in shape and separated simply by parallel shifts. In the present study, by contrast, the multiple trajectories observed for tBLG/*h*-BN were not all parallel and some even crossed each other. As defect-assisted tunneling spectroscopy is a local probe with a spatial extent of around a few nm, and earlier STS experiments probed AA stacking, AB stacking, and domain wall (DW) structures in tBLG, we suggest that our experimentally

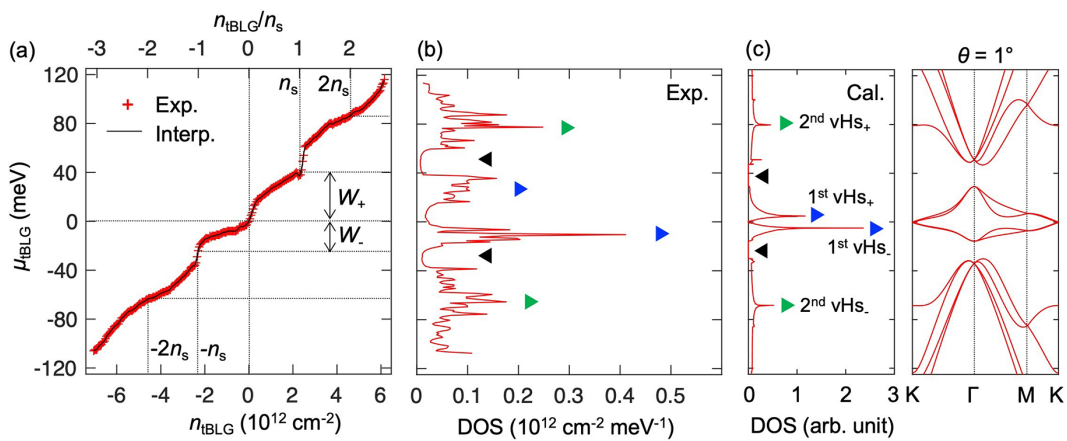


FIG. 3. (a) Experimental (red crosses) and interpolated (solid black line) plots of μ_{tBLG} vs n_{tBLG} extracted from resonant line I in Fig. 2(b). (b) DOS vs μ_{tBLG} obtained from (a). (c) Theoretical calculation of DOS (left) and band structure (right) for tBLG.

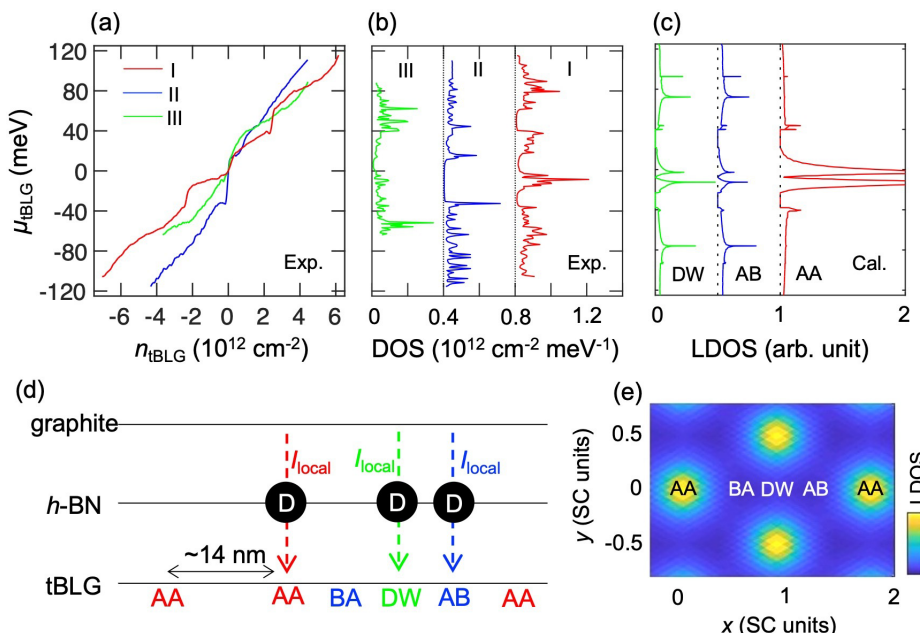


FIG. 4. (a) Plot of μ_{tBLG} vs n_{tBLG} extracted from resonant lines I, II, and III in Fig. 2(b). (b) DOS vs μ_{tBLG} obtained from (a). (c) Calculated local DOS vs μ_{tBLG} . (d) Schematic of defect-assisted tunneling at AA, AB/BA, and DW sites in tBLG. (e) Spatial distribution of calculated local DOS at the energy of first vHs₊ in tBLG.

derived three types of DOS correspond to the electronic states in local domains. Thus, we attribute the resonant lines and DOS color-coded red (I), blue (II), and green (III) to local defect-assisted tunneling and their local band structures at AA, AB/BA, and DW sites, respectively, in tBLG. For comparison, the calculated local DOS of AA, AB/BA, and DW sites in tBLG are shown in Fig. 4(c). Figure 4(d) schematically depicts defect-assisted tunneling at AA, AB/BA, and DW sites. Figure 4(e) shows the spatial distribution of local DOS in tBLG calculated using the method of Carr *et al.*⁴⁶

The DOS assigned to the AA site [Fig. 4(b), red] exhibits two distinct peaks on both sides of the CNP and gap-separated step-like structures at higher and lower energies. These features are consistent with the STS experiments, which revealed flat bands separated from the continuous levels by the energy gap, as well as the first and second vHs in both the conduction and valence bands.¹¹ The DOS assigned to the AB site (blue), having a Bernal-stacked BLG-like DOS shape, exhibits gap opening at the CNP with the application of a perpendicular electric field (Fig. S6). However, the DOS assigned to the DW region (green) has a singularity away from the CNP, and the gap at the CNP is not opened by the application of an electric field (Fig. S7). Qualitatively similar features were observed in STS experiments and theoretical calculations on small-angle tBLG.¹⁶ Various experiments and theories have reported the DOS in tBLG, some with contradictory results. The defect-assisted tunneling spectroscopy has the potential to be a powerful local probe, with excellent spatial and spectral resolution, that can be used to reveal the relationships between fascinating quantum transport phenomena and electronic band structures in twisted 2D vdW materials.

See the [supplementary material](#) for (1) the device characteristics, (2) the in-plane carrier transport characteristics of the MLG/h-BN reference device, (3) $\mu_{\text{tBLG}} - n_{\text{tBLG}}$ curves and DOS derived from all the trajectories, and (4) the bulk tunneling transport in the tBLG/h-BN device.

This work was supported by the JST-CREST, JST-Mirai, JST-PRESTO, and JST-SPRING (Grant Nos. JPMJCR15F3, JPMJCR20B4, JPMJMI21G9, JPMJPR20L5, and JPMJSP2108), JSPS KAKENHI (Grant Nos. JP19H02542, JP19H01820, JP20H00127, JP20H00354, JP21H05232, JP21H05233, and JP21H05234), the Kenjiro Takayanagi Foundation, the Inoue Foundation for Science, the Murata Science Foundation, the Advanced Technology Institute Research Grants, the Mazda Foundation, the Izumi Science and Technology Foundation, the Shorai Foundation for Science and Technology, and the Yazaki Memorial Foundation for Science and Technology.

AUTHOR DECLARATIONS

Conflict of Interest

The authors have no conflicts to disclose.

DATA AVAILABILITY

The data that support the findings of this study are available from the corresponding author upon reasonable request.

REFERENCES

- ¹Y. Cao, V. Fatemi, S. Fang, K. Watanabe, T. Taniguchi, E. Kaxiras, and P. Jarillo-Herrero, *Nature* **556**, 43 (2018).
- ²Y. Cao, V. Fatemi, A. Demir, S. Fang, S. L. Tomarken, J. Y. Luo, J. D. Sanchez-Yamagishi, K. Watanabe, T. Taniguchi, E. Kaxiras, R. C. Ashoori, and P. Jarillo-Herrero, *Nature* **556**, 80 (2018).
- ³X. Lu, P. Stepanov, W. Yang, M. Xie, M. A. Aamir, I. Das, C. Urgell, K. Watanabe, T. Taniguchi, G. Zhang, A. Bachtold, A. H. MacDonald, and D. K. Efetov, *Nature* **574**, 653 (2019).
- ⁴T. Cea, P. A. Pantaleón, and F. Guinea, *Phys. Rev. B* **102**, 155136 (2020).
- ⁵A. L. Sharpe, E. J. Fox, A. W. Barnard, J. Finney, K. Watanabe, T. Taniguchi, M. A. Kastner, and D. Goldhaber-Gordon, *Science* **365**, 605 (2019).
- ⁶M. Serlin, C. L. Tsirhart, H. Polshyn, Y. Zhang, J. Zhu, K. Watanabe, T. Taniguchi, L. Balents, and A. F. Young, *Science* **367**, 900 (2020).

- ⁷N. N. T. Nam and M. Koshino, *Phys. Rev. B* **96**, 075311 (2017).
- ⁸H. Yoo, R. Engelke, S. Carr, S. Fang, K. Zhang, P. Cazeaux, S. H. Sung, R. Hovden, A. W. Tsen, T. Taniguchi, K. Watanabe, G. C. Yi, M. Kim, M. Luskin, E. B. Tadmor, E. Kaxiras, and P. Kim, *Nat. Mater.* **18**, 448 (2019).
- ⁹A. Kerelsky, L. J. McGilly, D. M. Kennes, L. Xian, M. Yankowitz, S. Chen, K. Watanabe, T. Taniguchi, J. Hone, C. Dean, A. Rubio, and A. N. Pasupathy, *Nature* **572**, 95 (2019).
- ¹⁰Y. Jiang, X. Lai, K. Watanabe, T. Taniguchi, K. Haule, J. Mao, and E. Y. Andrei, *Nature* **573**, 91 (2019).
- ¹¹Y. Xie, B. Lian, B. Jäck, X. Liu, C. L. Chiu, K. Watanabe, T. Taniguchi, B. A. Bernevig, and A. Yazdani, *Nature* **572**, 101 (2019).
- ¹²Y. Choi, J. Kemmer, Y. Peng, A. Thomson, H. Arora, R. Polski, Y. Zhang, H. Ren, J. Alicea, G. Refael, F. von Oppen, K. Watanabe, T. Taniguchi, and S. Nadj-Perge, *Nat. Phys.* **15**, 1174 (2019).
- ¹³Y. Choi, H. Kim, Y. Peng, A. Thomson, C. Lewandowski, R. Polski, Y. Zhang, H. S. Arora, K. Watanabe, T. Taniguchi, J. Alicea, and S. Nadj-Perge, *Nature* **589**, 536 (2021).
- ¹⁴K. P. Nuckolls, M. Oh, D. Wong, B. Lian, K. Watanabe, T. Taniguchi, B. A. Bernevig, and A. Yazdani, *Nature* **588**, 610 (2020).
- ¹⁵M. Oh, K. P. Nuckolls, D. Wong, R. L. Lee, X. Liu, K. Watanabe, T. Taniguchi, and A. Yazdani, *Nature* **600**, 240 (2021).
- ¹⁶S. Huang, K. Kim, D. K. Efimkin, T. Lovorn, T. Taniguchi, K. Watanabe, A. H. Macdonald, E. Tutuc, and B. J. Leroy, *Phys. Rev. Lett.* **121**, 037702 (2018).
- ¹⁷N. Nilak, X. Lai, S. Wu, Z. Zhang, M. Xu, R. de A Ribeiro, P. C. Canfield, and E. Y. Andrei, *Nat. Commun.* **12**, 4180 (2021).
- ¹⁸J.-B. Qiao, L.-J. Yin, and L. He, *Phys. Rev. B* **98**, 235402 (2018).
- ¹⁹M. T. Greenaway, E. E. Vdovin, D. Ghazaryan, A. Misra, A. Mishchenko, Y. Cao, Z. Wang, J. R. Wallbank, M. Holwill, Y. N. Khanin, S. V. Morozov, K. Watanabe, T. Taniguchi, O. Makarovskiy, T. M. Fromhold, A. Patanè, A. K. Geim, V. I. Fal'ko, K. S. Novoselov, and L. Eaves, *Commun. Phys.* **1**, 94 (2018).
- ²⁰U. Chandni, K. Watanabe, T. Taniguchi, and J. P. Eisenstein, *Nano Lett.* **15**, 7329 (2015).
- ²¹Y. N. Khanin, E. E. Vdovin, M. V. Grigor'ev, O. Makarovskiy, M. Alhazmi, S. V. Morozov, A. Mishchenko, and K. S. Novoselov, *JETP Lett.* **109**, 482 (2019).
- ²²Y. Liu, Z. Tan, M. Kumar, T. S. Abhilash, G. J. Liu, and P. Hakonen, *APL Mater.* **6**, 091102 (2018).
- ²³D. Wong, J. Velasco, L. Ju, J. Lee, S. Kahn, H. Z. Tsai, C. Germany, T. Taniguchi, K. Watanabe, A. Zettl, F. Wang, and M. F. Crommie, *Nat. Nanotechnol.* **10**, 949 (2015).
- ²⁴I. Keren, T. Dvir, A. Zalic, A. Iluz, D. LeBoeuf, K. Watanabe, T. Taniguchi, and H. Steinberg, *Nat. Commun.* **11**, 3408 (2020).
- ²⁵S. Masubuchi, M. Morimoto, S. Morikawa, M. Onodera, Y. Asakawa, K. Watanabe, T. Taniguchi, and T. Machida, *Nat. Commun.* **9**, 1413 (2018).
- ²⁶M. Onodera, S. Masubuchi, R. Moriya, and T. Machida, *Jpn. J. Appl. Phys.* **59**, 010101 (2020).
- ²⁷K. Kim, M. Yankowitz, B. Fallahazad, S. Kang, H. C. P. Movva, S. Huang, S. Larentis, C. M. Corbet, T. Taniguchi, K. Watanabe, S. K. Banerjee, B. J. Leroy, and E. Tutuc, *Nano Lett.* **16**, 1989 (2016).
- ²⁸Y. Cao, J. Y. Luo, V. Fatemi, S. Fang, J. D. Sanchez-Yamagishi, K. Watanabe, T. Taniguchi, E. Kaxiras, and P. Jarillo-Herrero, *Phys. Rev. Lett.* **117**, 116804 (2016).
- ²⁹J. M. Park, Y. Cao, K. Watanabe, T. Taniguchi, and P. Jarillo-Herrero, *Nature* **592**, 43 (2021).
- ³⁰Y. Seo, S. Masubuchi, E. Watanabe, M. Onodera, R. Moriya, K. Watanabe, T. Taniguchi, and T. Machida, *Appl. Phys. Lett.* **117**, 243101 (2020).
- ³¹R. K. Kumar, X. Chen, G. H. Auton, A. Mishchenko, D. A. Bandurin, S. V. Morozov, Y. Cao, E. Khestanova, M. ben Shalom, A. V. Kretinin, K. S. Novoselov, L. Eaves, I. V. Grigorieva, L. A. Ponomarenko, V. I. Fal'ko, and A. K. Geim, *Science* **357**, 181 (2017).
- ³²S. Jung, N. Myoung, J. Park, T. Y. Jeong, H. Kim, K. Watanabe, T. Taniguchi, D. H. Ha, C. Hwang, and H. C. Park, *Nano Lett.* **17**, 206 (2017).
- ³³H. Kim, N. Leconte, B. L. Chittari, K. Watanabe, T. Taniguchi, A. H. Macdonald, J. Jung, and S. Jung, *Nano Lett.* **18**, 7732 (2018).
- ³⁴A. Mishchenko, J. S. Tu, Y. Cao, R. V. Gorbachev, J. R. Wallbank, M. T. Greenaway, V. E. Morozov, S. V. Morozov, M. J. Zhu, S. L. Wong, F. Withers, C. R. Woods, Y. J. Kim, K. Watanabe, T. Taniguchi, E. E. Vdovin, O. Makarovskiy, T. M. Fromhold, V. I. Fal'ko, A. K. Geim, L. Eaves, and K. S. Novoselov, *Nat. Nanotechnol.* **9**, 808 (2014).
- ³⁵M. T. Greenaway, E. E. Vdovin, A. Mishchenko, O. Makarovskiy, A. Patanè, J. R. Wallbank, Y. Cao, A. V. Kretinin, M. J. Zhu, S. V. Morozov, V. I. Fal'ko, K. S. Novoselov, A. K. Geim, T. M. Fromhold, and L. Eaves, *Nat. Phys.* **11**, 1057 (2015).
- ³⁶J. R. Wallbank, D. Ghazaryan, A. Misra, Y. Cao, J. S. Tu, B. A. Piot, M. Potemski, S. Pezzini, S. Wiedmann, U. Zeitler, T. L. M. Lane, S. V. Morozov, M. T. Greenaway, L. Eaves, A. K. Geim, V. I. Fal'ko, K. S. Novoselov, and A. Mishchenko, *Science* **353**, 575 (2016).
- ³⁷E. E. Vdovin, A. Mishchenko, M. T. Greenaway, M. J. Zhu, D. Ghazaryan, A. Misra, Y. Cao, S. V. Morozov, O. Makarovskiy, T. M. Fromhold, A. Patanè, G. J. Slotman, M. I. Katsonel, A. K. Geim, K. S. Novoselov, and L. Eaves, *Phys. Rev. Lett.* **116**, 186603 (2016).
- ³⁸S. Jung, M. Park, J. Park, T. Y. Jeong, H. J. Kim, K. Watanabe, T. Taniguchi, D. H. Ha, C. Hwang, and Y. S. Kim, *Sci. Rep.* **5**, 16642 (2015).
- ³⁹D. A. Ghazaryan, A. Misra, E. E. Vdovin, K. Watanabe, T. Taniguchi, S. V. Morozov, A. Mishchenko, and K. S. Novoselov, *Appl. Phys. Lett.* **118**, 183106 (2021).
- ⁴⁰Y. Seo, S. Masubuchi, M. Onodera, Y. Zhang, R. Moriya, K. Watanabe, T. Taniguchi, and T. Machida, *Appl. Phys. Lett.* **120**, 083102 (2022).
- ⁴¹M. Onodera, M. Isayama, T. Taniguchi, K. Watanabe, S. Masubuchi, R. Moriya, T. Haga, Y. Fujimoto, S. Saito, and T. Machida, *Carbon* **167**, 785 (2020).
- ⁴²M. Onodera, K. Watanabe, M. Isayama, M. Arai, S. Masubuchi, R. Moriya, T. Taniguchi, and T. Machida, *Nano Lett.* **19**, 7282 (2019).
- ⁴³U. Chandni, K. Watanabe, T. Taniguchi, and J. P. Eisenstein, *Nano Lett.* **16**, 7982 (2016).
- ⁴⁴L. Britnell, R. V. Gorbachev, R. Jalil, B. D. Belle, F. Schedin, A. Mishchenko, T. Georgiou, M. I. Katsonel, L. Eaves, S. V. Morozov, N. M. R. Peres, J. Leist, A. K. Geim, K. S. Novoselov, and L. A. Ponomarenko, *Science* **335**, 947 (2012).
- ⁴⁵L. A. Ponomarenko, B. D. Belle, R. Jalil, L. Britnell, R. V. Gorbachev, A. K. Geim, K. S. Novoselov, A. H. Castro Neto, L. Eaves, and M. I. Katsonel, *J. Appl. Phys.* **113**, 136502 (2013).
- ⁴⁶S. Carr, S. Fang, Z. Zhu, and E. Kaxiras, *Phys. Rev. Res.* **1**, 013001 (2019).
- ⁴⁷Z. Zhang, R. Myers, K. Watanabe, T. Taniguchi, and B. J. LeRoy, *Phys. Rev. Res.* **2**, 33181 (2020).
- ⁴⁸D. Wong, K. P. Nuckolls, M. Oh, B. Lian, Y. Xie, S. Jeon, K. Watanabe, T. Taniguchi, B. A. Bernevig, and A. Yazdani, *Nature* **582**, 198 (2020).